Crack Growth Rate at Oxygen Electrode/Electrolyte Interface in Solid Oxide Electrolysis Cells Predicted by Experiment Coupled Multiphysics Modeling

Puvikkarasan Jayapragasam,[1] Yeting Wen,[2] Korey Cook,[1,3] Jacob A. Wrubel,[3]
Zhiwen Ma,[3] Kevin Huang,[2,*] and Xinfang Jin[1,*,z]

[1]*Mechanical Engineering Department, University of Massachusetts, Lowell, Massachusetts 01854, United States of America*
[2]*Mechanical Engineering Department, University of South Carolina, Columbia, South Carolina 29201, United States of America*
[3]*National Renewable Energy Laboratory, Golden, Colorado 80401, United States of America*

Solid oxide electrolysis cell (SOEC) is a very efficient hydrogen production technology, but the cell degradation is a serious limiting factor for its long-term implementation. Oxygen electrode (OE) delamination is reported to be the critical degradation mechanism. In this study, we present a methodology to understand the delamination failure of the OE due to chemical stress in a better perspective. Several OE configurations were tested: baseline strontium-doped lanthanum cobalt iron oxide (LSCF) single layer design and tantalum-doped strontium cobalt oxide (SCT) - LSCF bilayer designs with different SCT loadings. An electro-chemo-mechanical model is developed to associate the electrochemical behavior of the cell with solid mechanics for calculating crack growth of the cell during long term test. The bilayer configuration with SCT 20 wt% has better performance as it survived in the long-term life test with the least crack length. This study implies that an additional nano-coating of SCT over the OE have improved the species transport and oxygen evolution with reduced chemical stress. As the operating current density decreases, it takes longer time for the cell to reach the delamination with the same critical crack length of 6.5 μm (~93% of the electrode/electrolyte interface length). Finally, it was concluded that chemical stress plays a significant role in interface delamination failure, however it may not be the only source of stresses at the interface.

List of Symbols

Greek Symbols

σ_k	Conductivity of material k
σ_{ij}	Stress
β	Symmetry factor
Γ	J-integral domain
β^c	Chemical expansion co-efficient
δ	Oxygen Stoichiometry
η	Surface overpotential
ϕ	Potential
μ	Electrochemical potential
υ	Poisson's ratio
ε_{ij}	Strain

Symbols

c_k	Molar concentration of species k (mol/m³)
D	Diffusivity (m²/s)
E	Young's modulus (Pa)
e	Electron
E_{eq}	Equilibrium potential (V)
exp	Exponential function
F	Faraday's constant (96485 C mol⁻¹)
h	Hole
i_{ex}	Exchange current density (A/m²)
J	Current density (A/m²)
J_k	Molar flux of element k (mol/m²s)
k_{chem}	Reaction kinetics
K_I	Stress intensity factor
n	Charge
R	universal gas constant (8.314 J mol⁻¹ K⁻¹)
r	Radius (m)
T	Temperature (K)
t	Time in long term test (h)

V	Vacancy
V_{cell}	Operating cell voltage (V)
V_m	Molar Volume (m³/mol)
z	Effective Charge
u	Displacement vector
J	J-integral (J/m²)
Tr	Traction vector perpendicular to Γ

Superscript

..	+2 charge (Kröger-Vink notation)
.	+1 charge (Kröger-Vink notation)
"	−2 charge (Kröger-Vink notation)
'	−1 charge (Kröger-Vink notation)
x	Neutral charge (Kröger-Vink notation)

Subscripts

chem	Chemical reaction
eq	Equilibrium
e	Electron
GDC	GDC layer
GTPB	TPB in GDC layer
GL	GDC/LSCF DPB
GLe	Electron hole in GDC/LSCF DPB
GLV	Vacancy in GDC/LSCF DPB
h	Electron hole
i	Interstitial
LSCF	LSCF layer
O	Lattice Oxygen
V	Vacancies

Solid oxide electrolyzer cells (SOECs), which are electrochemical devices that convert electricity into hydrogen, have received widespread attention as a means of multi-day or seasonal energy storage approach to enable the integration of intermittent renewable energy into the grid.[1] Despite tremendous materials developments and performance improvements of the technology in the past decade,[1] challenges remain in understanding its degradation mechanism, including nickel relocation in H_2 electrode,[2] solid-solid

*Electrochemical Society Member.
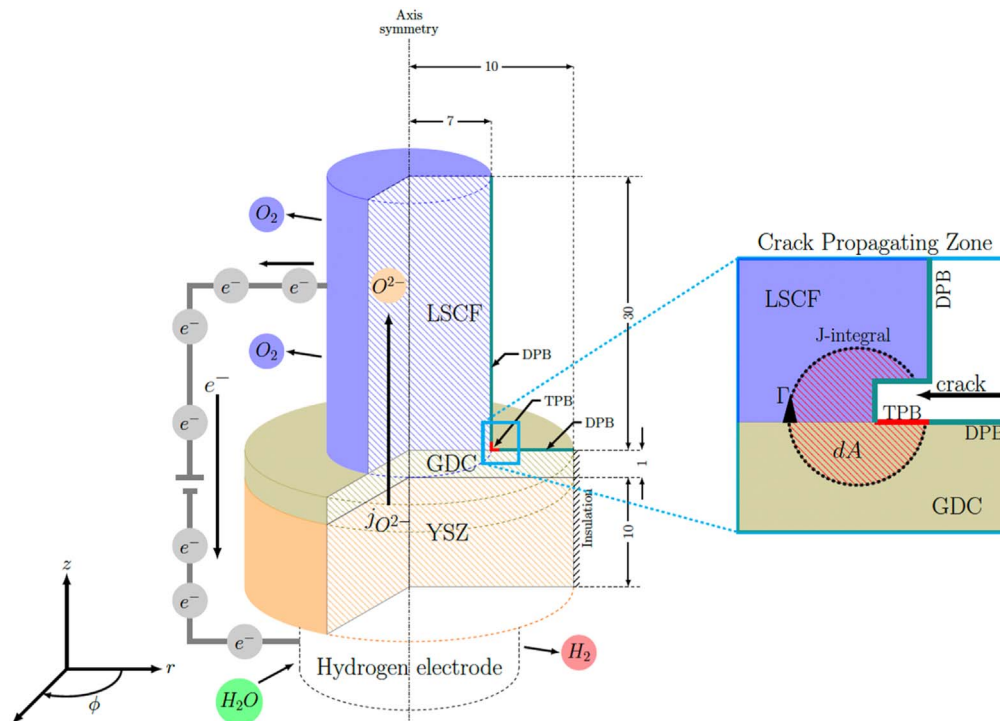zE-mail: Xinfang_Jin@uml.edu

Figure 1. Schematic illustration of microscale cell in electrolysis mode with illustrated boundary conditions and crack used in computation. All dimensions are in μm.

interface interdiffusion and segregation of cations,[3] electrode chromium poisoning,[2,4,5] and the delamination of O_2 electrode/electrolyte (OE/EL) interface.[6–8] Present research efforts are focused on developing new OEs that can decelerate the degradation and extend the stack lifetime beyond 60,000 h at 1.5 A cm^{-2}, which will significantly drive the stack price down to \$100/kW and hydrogen cost down to \$2 kg^{-1}.[9]

Delamination of the OE from the EL is one of the major drivers for SOEC performance degradation, leading to severe performance loss beyond 1000 h[8,10] and becoming a technical barrier for its commercialization.[11] The degradation rate of SOEC is two times faster than that of a similar cell under fuel cell operation.[12] Efforts have been made by researchers to understand and eliminate the delamination effect. Several delamination mechanisms have been proposed and one of such mechanisms is the development of a pre-existing minor crack or expansion of a pore at OE/EL interface into crack due to accumulation of oxygen partial pressure.[8,13,14] Researchers also found that the migration of oxygen ions from electrolyte leading to the formation of nano particles at OE can affect its lattice structure and result in delamination.[10] Similarly, it was noted that formation of grain boundaries at OE/EL interface deteriorates ohmic and polarization resistances of the cell and in the long run results in delamination.[15] Inter-diffusion and segregation of cations (like Sr in LSCF electrode) at OE/EL interface that reduces oxygen surface exchange rate at electrode surfaces can be additional cause for delamination.[3,11,16] In the present work, it is considered that lattice oxygen stoichiometry variation at the interface of the OE/EL causes lattice structural contraction and eventually leads to delamination.[17]

Mixed electronic and ionic conductors (MIECs) such as $La_{1-x}Sr_xCo_{1-y}Fe_yO_{3-\delta}$ (LSCF) are common OE of choice for SOECs. One of the advantages of the MIEC is that it extends the electrochemically active sites to the entire electrode instead of limiting them to triple phase boundary (TPB –i.e., the boundary where electrode, electrolyte, and gas phase meet).[3] Moreover, OE

delamination and oxygen bubble formations were not normally seen in SOECs with LSCF.[18,19] However, such cells still suffer from short lifetimes with current densities over 1 A cm^{-2}. In our early work,[17] we showed through parametric studies that LSCF skeleton coated with SCT ($SrCo_{0.9}Ta_{0.1}O_{3-\delta}$) layer (denoted as bilayer design) exhibits a significantly higher oxygen evolution rate than LSCF only (termed as single layer baseline design). The bilayer OE design inherently alleviates delamination owing to their fast oxygen evolution reaction (OER) rate.

In this study, we further investigate the effects of four different SCT loadings on the performance of the bilayer design and compare them with the single layer baseline LSCF design. We implement electro-chemo-mechanically coupled model to correlate the length of chemical-stress-induced cracks at the OE/EL interface with cell current density and evaluate its crack growth rate during a long-term polarization test. The crack growth rate and variations of crack length as a function of operating duration and current density are the major outcomes of this modeling work.

This paper is organized as follows. Mathematical model section gives the details about the mathematical model including the equations governing the transport of oxygen vacancies, holes, and electrons. Solid mechanics are solved with J-integral to evaluate failure caused by chemical stress from oxygen stoichiometry variation. Experimental Validation and Model Parameters section describes the validation of the model using experimentally obtained voltage-current density curve (V-I curve). Results section compares the electrochemical performance of baseline and bilayer OE designs by analyzing the cell V-I curves and the ratio of current contribution by DPB (double-phase boundary) and TPB pathways. The concentrations of oxygen vacancies and interstitial oxygen were also computed as these are responsible for lattice oxygen variation. Later, the model results were correlated with experimental data to obtain crack length variation as a function of time for different OE configurations polarized under 1 A cm^{-2}. Lastly, model simulation was extended for bilayer OE design operated at different current densities.

Mathematical Model

The 3D representation of the microstructure of porous mixed conducting OE is complicated and nontrivial to implement. As a compromise, a uniform array of identical cylindrical rods arranged in a circular grid[20] could be used to represent the porous structure. Due to the high electronic conductivity in the MIEC electrode, it is assumed that the entire electrode stack will be in isopotential. This narrows down the computational domain from the array of cylindrical rod stack to a single rod. A schematic representation of the modeling domain considered in the work is shown in Fig. 1.

The cylindrical geometry is used to gain insights on the transport process and delamination failure of the cell, particularly in OE.[21] Different configurations of OEs are considered in this work: commonly used LSCF[22] is chosen as the baseline single layer OE design, and LSCF OE with SCT coating of 10, 15, 20 and 25 wt% as bilayer design. The thickness of SCT layer over LSCF is on the order of a few nanometers and hence, SCT layer thickness becomes negligible compared to dimensions of the bulk OE (in microns). Consequently, the geometry used in computation is identical for both single layer baseline and bilayer configurations, but different parameter values are used to account for the effect on the reaction kinetics on OE surface.

Model details.—Two types of multiphase boundaries exist in the electrode structure: double-phase boundaries (DPB) and triple phase boundaries (TPB). The relevant DPBs include GDC/LSCF, YSZ/GDC, LSCF/Gas and GDC/Gas. The TPBs are located at the intersection of the Gas, LSCF (electrode) and GDC (electrolyte-buffer layer). The length of the TPB segment is chosen carefully to symbolize the actual TPB length computed by analyzing the tomographic image data of the electrode.[23]

Figure 1 illustrates the position of multiphase boundaries on the external surface of the OE and buffer layer. Lattice oxygen in both LSCF and GDC phases can be liberated to the pore phase as free oxygen atoms through a combination of the oxygen evolution reaction (OER) and oxygen desorption reaction (ODR). A detailed explanation about these reactions is provided in our previous work.[17] To make this article self-explanatory, the governing equations with boundary conditions are listed in Table I. These governing equations specify transport of charged species, such as oxygen vacancies ($V_o^{··}$), electron (e') and hole (h˙) expressed using Kröger-Vink notations,[24] within the electrolysis cell. The overpotential at YSZ/Ni-GDC ($\eta_{s,YGN}$) is back-calculated by Butler-Volmer's equation in COMSOL such that the current density ($i_{V,YSZ}$) is equivalent to desired current density.

Our previous work[17] showed that there are two oxide ion transport pathways: DPBs and TPBs. The competition between chemical reaction kinetics in DPBs and electrochemical kinetics in TPBs is closely correlated to the lattice oxygen stoichiometry variation, which becomes the primary reason for chemical contraction of lattice structures at the interface and ultimately leads to delamination of OE. Enhancing the kinetics of the DPB pathway can help to alleviate the delamination. The results from the earlier work[17] showed that the additional layer of SCT on OE (bilayer design) improves the reaction kinetics at DPBs compared to the single layer design.

The prior developed numerical model was used to investigate the oxygen stoichiometry variation for different current densities and different reaction kinetics.[17] In this research, the numerical model was further comprehended to simulate crack development at OE/EL interface and to investigate its impact on the electrochemical performance. It is assumed that the crack is initiated at the outer OE/EL interface where TPB occurs and further develops to reach the center of the cylinder. J-integral and stress intensity factor are employed as the fracture criteria to evaluate the crack growth rate. The J-integral contour is formed around the crack tip and moved along with the advancement of the crack tip. The propagation of the crack shrinks the LSCF/GDC interfacial region and introduces additionally new LSCF/Gas interfacial region as shown in Fig. 1 (enlarged one in the right). Since the geometry considered here is axis symmetric, the 3D cylindrical model is simplified to a 2D axial symmetric model by considering a plane at a particular ϕ axis in the cylindrical coordinate.

Mechanical and chemical stress - strain.—The mechanical strain induced by stress σ_{ij} on an isotropic elastic material is given by:[25]

$$\varepsilon_{ij}^M = \frac{1}{E}[(1 + \nu)\sigma_{ij} - \nu\sigma_{kk}\delta_{ij}] \qquad [1]$$

Here E is young's modulus of the material and ν is Poisson's ratio. The strain induced by chemical stress due to oxygen vacancy variation in the cell is given as:[26]

$$\varepsilon_{ij}^C = \beta^c \Delta c \delta_{ij} \qquad [2]$$

Where Δc is the concentration variation of lattice oxygen caused by oxygen vacancies and oxygen interstitials referenced to the perfectly stoichiometric state and β^c is an isotropic chemical expansion/contraction coefficient which is analogous to a thermal expansion coefficient. The total strain experienced by the body due to combined contribution of mechanical and chemical stress is,

$$\varepsilon_{ij} = \frac{1}{E}[(1 + \nu)\sigma_{ij} - \nu\sigma_{kk}\delta_{ij}] + \beta^c \Delta c \delta_{ij} \qquad [3]$$

The stress vector is expressed using the above presented mechanical and chemical strain components as:[25]

$$\sigma_{ij} = \frac{E}{(1 + \upsilon)}\varepsilon_{ij} + \frac{E\upsilon}{(1 - 2\upsilon)(1 + \upsilon)}\varepsilon_{kk}\delta_{ij} \\ - \frac{\beta^c E}{(1 + \upsilon)}\left\{1 + \frac{3}{(1 - 2\upsilon)}\right\}\Delta c \delta_{ij} \qquad [4]$$

For isotropic elastic body, strain components can be related to displacement u as following,[27]

$$\varepsilon_{ij} = \frac{1}{2}\left(\frac{\partial u_r}{\partial r} + \frac{\partial u_z}{\partial z}\right) \qquad [5]$$

Stress and strain can be induced due to unit cell variations which results in chemical expansion or contraction.

The effect of inherent residual thermal stress in the electrode is elaborated in appendix B. The residual stress superimposes with the chemical-induced stress[28] and can be expressed similar to chemical strain, as

$$\varepsilon_{ij}^R = \beta^T \Delta T \qquad [6]$$

ΔT is difference between operating temperature and the sintering temperature (stress-free) of the electrode, and β^T is thermal expansion/contraction coefficient.

J integral.—The crack development at the oxygen electrode/electrolyte (OE/EL) interface is illustrated in Fig. 1. A circular contour Γ with diameter of 0.3 μm and area dA was constructed around the tip of the crack to evaluate J-integral. It has been shown that the J-integral taken along any unclosed contour between unloaded crack surfaces is path independent.[29,30] Even though considerable plasticity may occur near the vicinity of the crack tip, any path sufficiently far from the crack tip can be selected to conveniently analyze fracture mechanics.

J-integral over two-dimensional contour Γ surrounding the crack tip is defined as:[29–31]

Table I. Governing equations and boundary conditions.

Domain	Governing equation	Interface	Boundary conditions
YSZ	$\nabla.\left(\underbrace{\dfrac{\sigma_k}{Fz_v}\nabla\phi}_{i_{v,YSZ}}\right)=0$	YSZ/Ni-GDC	$i_{V,YSZ}=\dfrac{i_{oc}}{Fz_v}\left[\exp\left(\dfrac{(1-\beta)z_vF}{RT}\eta_{s,YGN}\right)\right.$ $\left.-\exp\left(\dfrac{-\beta z_vF}{RT}\eta_{s,YGN}\right)\right]$ $\phi_{eq}=0$
GDC	$\nabla.\left(\underbrace{-D_{V,GDC}\left(\nabla c_{V,GDC}+\dfrac{z_vF}{RT}c_{V,GDC}\nabla\phi\right)}_{i_{v,GDC}}\right)=0$	YSZ/GDC	$i_{V,YSZ}=i_{V,GDC},\,\phi_{YSZ}=\phi_{GDC}$
		YSZ/GDC	$i_{V,YSZ}=i_{V,GDC},\,\phi_{YSZ}=\phi_{GDC},\,i_{e,GDC}=0$
		GDC/O$_2$	$i_{V,GDC}=k_{chem}(c^0_{V,GDC}-c_{V,GDC})$ $i_{e,GDC}=2k_{chem}(c^0_{V,GDC}-c_{V,GDC})$
		GDC/LSCF/O$_2$	$i_{V,G3PB}=\dfrac{i_{oa3}}{Fz_v}\left[\exp\left(\dfrac{(1-\beta)z_vF}{RT}\eta_{s,G3PB}\right)\right.$ $\left.-\exp\left(\dfrac{-\beta z_vF}{RT}\eta_{s,G3PB}\right)\right]$ $\eta_{s,G3PB}=V_{cell}-\phi_{GDC}-E_{eq},\,i_{e,GDC}=0$
	$\nabla.\left(\underbrace{-D_{e,GDC}\left(\nabla c_{e,GDC}+\dfrac{z_eF}{RT}c_{e,GDC}\nabla\phi\right)}_{i_{e,GDC}}\right)=0$	GDC/LSCF	$i_{V,GL}=\dfrac{i_{oa2}}{Fz_v}\left[\exp\left(\dfrac{(1-\beta)z_vF}{RT}\eta_{s,GLV}\right)\right.$ $\left.-\exp\left(\dfrac{-\beta z_vF}{RT}\eta_{s,GLV}\right)\right]$ $\eta_{s,GLV}=\dfrac{\mu_{V,LSCF}-\mu_{V,GDC}}{z_VF}-E_{eq}$ $i_{e,GL}=\dfrac{i_{oa2}}{Fz_e}\left[\exp\left(\dfrac{(1-\beta)z_eF}{RT}\eta_{s,GLe}\right)\right.$ $\left.-\exp\left(\dfrac{-\beta z_eF}{RT}\eta_{s,GLe}\right)\right]$ $\eta_{s,GLe}=\dfrac{\mu_{h,LSCF}+\mu_{e,GDC}}{z_hF}-E_{eq}$
LSCF	$\nabla.(\underbrace{-D_{V,LSCF}(\nabla c_{V,LSCF})}_{i_{v,LSCF}})=0$	LSCF/O$_2$	$r_{evo}=k_{evo}\left\{\dfrac{(1-\theta_s)}{(1-\theta_0)}\times\dfrac{c_{h,LSCF}}{c^0_{h,LSCF}}\exp\left(\dfrac{\beta z_vF}{RT}\Delta\chi_h\right)\right.$ $\left.-\dfrac{\theta_s}{\theta_0}\times\dfrac{c_{V,LSCF}}{c^0_{V,LSCF}}\exp\left(-\dfrac{(1-\beta)z_vF}{RT}\Delta\chi_h\right)\right\}$ $r_{des}=k_{desf}\theta_0^2-k_{desb}P_{O_2}\theta_s^2$ $i_{V,LSCF}=r_{evo},\,i_{V,LSCF}=r_{des}$
	$\nabla.(-D_{V,LSCF}\nabla c_{i,LSCF})=0$	LSCF/GDC	$i_{V,LSCF}=i_{V,GL}$
		Boundaries	$c_{i,LSCF}=\delta/V_{m,LSCF}$

$$J_1=\int_\Gamma Wdz-Tr\frac{\partial u}{\partial r}ds \qquad [7]$$

where, Strain energy $W=\frac{1}{2}(\sigma_r.\varepsilon_r+\sigma_z.\varepsilon_z+\sigma_\phi.\varepsilon_\phi+\sigma_{rz}.2\varepsilon_{rz})$,

Traction $Tr\dfrac{\partial u}{\partial r}=\begin{bmatrix}\sigma_r.n_r+\sigma_{rz}.n_z\\ \sigma_{rz}.n_r+\sigma_z.n_z\end{bmatrix}\begin{bmatrix}\dfrac{\partial u_r}{\partial r} & \dfrac{\partial u_z}{\partial r}\end{bmatrix}$,

The above J-integral relation in Eq. 7 is suitable only for homogenous structure and cannot be extended to the present work as the crack propagates at a bi-material interface. Some of the researchers claim that modification is required in J-integral calculation unless the bonding between the materials is straight.[32]

For accurate estimation, J-integral in Eq. 7 needs to adapt the jump in the energy density and displacement between the materials at the interface and crack opening.[33,34] Figure 2a gives an overview of how J-integral contour is constructed for bi-material interfacial

crack. It is assumed that the cracked surface is traction free and, displacement and traction have the continuity at the interface. Two additional integral paths are taken, one near the interface (Γ_i) and second near crack opening (Γ_c) region.

$$J_c=\int_{\Gamma_c}[W]d\Gamma$$

$$J_i=\int_{\Gamma_i}([W]-\sigma_{jz}[u_z])d\Gamma$$

$$J_{2Q}=J_1-J_c-J_i \qquad [8]$$

The integral J_c provides the energy density jump at the crack surface and integral J_i gives variation of traction and energy at the interface. The modified integral $J_{2\rho}$ in Eq. 8 provides the energy release rate of
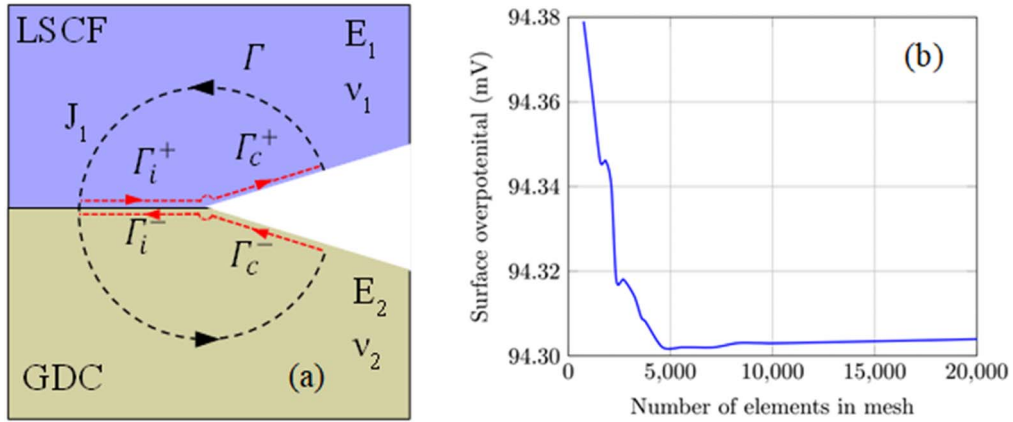
Figure 2. Integral pathway and direction for J-integral at bi-material interface (a) and Mesh convergence study (b) – influence of number of elements over surface overpotential.

the crack tip which excludes the potential energy jump at the crack surface and interface. The variables W and u_z, in the form [X] presents the difference in their values at the interface as $X(r, z_i^+)$—$X(r, z_i^-)$. Here z_i is the position of the interface in the z-coordinate and, superscript + and—indicates the region closer to the interface in LSCF and GDC domain respectively.

The modified stress intensity factor is presented in complex form as $K_I = K_1 - iK_2$ with $i = -1^2$.[33–35] The J-integrals from Eqs. 7 and 8 aids in solving the following quadratic equation,

$$K_1^4(4C_1^2 + 4C_2^2) - 4K_1^2[J_1B_1(C_1^2 + C_2^2) + J_{2\varrho}C_1] + (J_1B_1C_1 + J_{2\rho})^2 = 0 \qquad [9]$$

$$(K_1^2 + K_2^2) = B_1J_1 \qquad [10]$$

The coefficients in the above equations are given as,

$$\frac{1}{B_1} = \left[\frac{(1 + \kappa_1)}{16\mu_1} + \frac{(1 + \kappa_2)}{16\mu_2}\right]$$

$$C_1 = -\frac{1}{32\pi\epsilon}\left[\frac{(1 + \kappa_1)}{\mu_1}(1 - e^{-2\pi\epsilon}) + \frac{(1 + \kappa_2)}{\mu_2}(e^{-2\pi\epsilon} - 1)\right]\sin(2\epsilon\log\varrho)$$

$$C_2 = -\frac{1}{32\pi\epsilon}\left[\frac{(1 + \kappa_1)}{\mu_1}(1 - e^{-2\pi\epsilon}) + \frac{(1 + \kappa_2)}{\mu_2}(e^{-2\pi\epsilon} - 1)\right]\cos(2\epsilon\log\varrho)$$

Where subscript 1 and 2 in the Eqs. 9–10 represents LSCF and GDC respectively, $\kappa_k = (3 - 4\nu_k)/(1 + \nu_k)$, bi-material constant $\epsilon = \frac{1}{2\pi}\ln\left[\frac{\kappa_1\mu_2 + \mu_1}{\kappa_2\mu_1 + \mu_2}\right]$, μ_k is shear modulus and ν_k is Poisson's ratio for the material k.

Using Eqs. 7–10, the stress intensity factor K_I is calculated and compared with the fracture toughness of the material K_{IC} to evaluate the failure criteria. The direction of contour Γ in the cracked solid is pointed from the bottom to the top of the crack surface.

The governing equations presented in Table I are coupled with solid mechanics, given by Eqs. 1–10, and are solved in COMSOL 6.0 ® using the coefficient form PDE in mathematical module and structural mechanics module.

The computational domain is meshed using free triangular mesh and mesh convergence study was conducted using overpotential at OE/EL interface as the measuring factor. From Fig. 2b, it seems that the overpotential becomes invariable for elements more than 6500. So, the computational domain is meshed with total 7500 triangular elements which takes 13 seconds of computational time to solve equations for a particular crack length and current density. The critical value of delamination is arbitrarily chosen as 6.5 μm since it reaches more than 90% of the OE radius, which is 7 μm (as shown in Fig. 1).

Experimental Validation and Model Parameters

The experimental data is measured with symmetric cells using two different OE configurations: LSCF single layer design (baseline); LSCF/SCT bilayer design with different SCT loading percentages. In the model, the conductivity and diffusivity for the charge species (like electron, vacancy, hole, etc.) in the materials were taken from previous study.[17] The electrochemical and reaction kinetic parameters are the factors which distinguish the performance of different OE electrode configurations. Therefore, the parameter vector $\alpha_i = [i_{oa2}, i_{oa3}, k_{desb}, k_{desf}, k_{evo}, \beta]$ characterizing DPB and TPB surface reaction kinetics are estimated using experimentally measured VI curve.

Sensitivity analysis is performed by taking the first derivative of the overpotential with respect to parameters for the corresponding current density using complex step differentiation (CSD).[36] Figure 3a gives the normalized sensitivity for intact cell computed using Eq. 11. In the equation, $\mathfrak{I}\{\}$ is a function returning imaginary part of complex variable, h is small step size (chosen as 10^{-6}).

$$X_\alpha = \alpha_j\frac{\partial\eta}{\partial\alpha_j} = \alpha_j\frac{\mathfrak{I}\{\eta(\alpha_j + ih)\}}{h} \qquad [11]$$

The parameters like oxygen desorption rate - both forward and backward are found to be insensitive which makes the simultaneous estimation of these parameters a tedious task. The sensitivities of other parameters like exchange current densities at DPB and TPB, oxygen evolution rate kinetics and symmetry factor are high.

Correlation analysis was performed to evaluate any linear dependency among the parameters and pointed out that DPB exchange current density is highly correlated with reaction kinetics of oxygen desorption and evolution rates, and all the reaction rate constants are highly correlated as shown in Fig. 3b. Further explanation and discussion on correlation analysis and procedure for approximating the unknown parameters are given in appendix A.
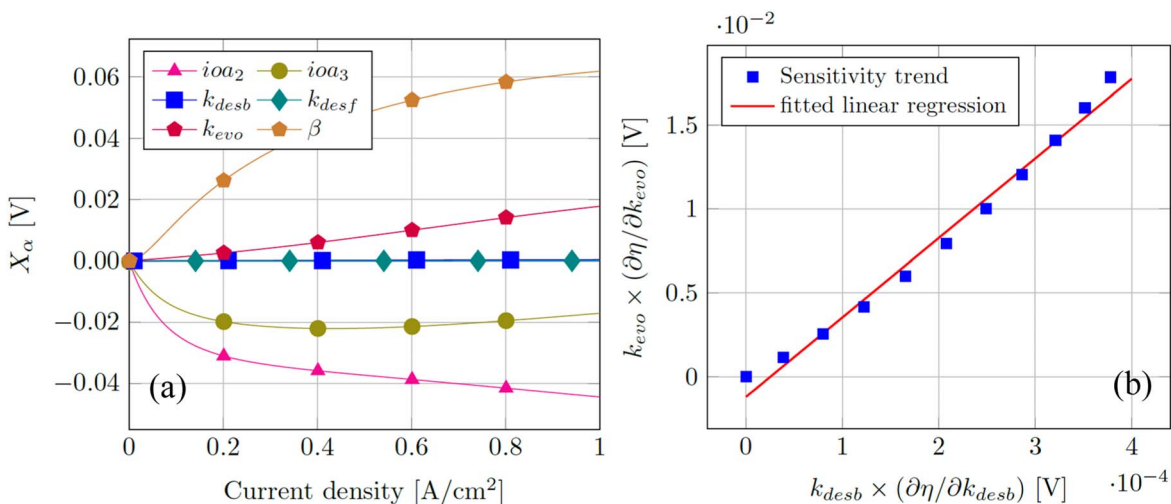
Figure 3. Scaled sensitivity profiles for overpotential with respect to parameters (a) and correlation analysis between oxygen evolution reaction rate and backward desorption reaction rate with linear regression (b).

It is concluded that the parameters: DPB and TPB exchange current density, oxygen evolution rate and symmetry factors, can be approximated simultaneously with experimental measurements.

The estimated parameters for all OE configurations are presented in Table II. It can be observed from the table that the parameters associated with both DPB, and TPB interface reaction kinetics are enhanced in the bilayer design and the enhancement is dependent of SCT loading. With 20 wt% SCT loading, the electrochemical performance of the cell has reached its maximum. Therefore, 20 wt% SCT/LSCF bilayer OE design is considered as the optimal electrode for electrolysis applications among all the configurations tested in this study. The second step of validation for predicting crack growth rate will be discussed more in a later section.

Results

Results from the model analysis are presented in three parts as: 1) Impact of crack length on the electrochemical and mechanical performance, 2) crack growth rate during life cycle test and 3) model prediction for different current densities.

Electrochemical—mechanical performance with crack.—As shown in Fig. 1, a crack has been manually constructed at the OE/EL interface. The length of the crack was varied from 0.5 to 6.5 μm to study its effect on the electrochemical performance of the cell (e. g., V-I curve and current ratio between TPB and DPB pathways). With a 6.5 μm crack, the OE almost completely detached from the electrolyte layer. The electrochemical and mechanical performance of the cell were analyzed for various crack lengths and operating voltages of the single layer baseline and bilayer OE designs. For the sake of brevity, only the SCT 20 wt% loading was used to compare the bilayer design with the single layer design. In the following sections, the simulation results are presented with symbols in the figures to easily distinguish and compare them.

Single layer—baseline design.—Figure 4a illustrates concentration of oxygen interstitial, which is an oxygen surplus relative to the equilibrium before current loading, at the OE/EL interface for the single layer OE design. The oxygen interstitial concentration increases from 2.5 mol m^{-3} to 6.5 mol m^{-3} as the operating voltage increases from 1.12 to 1.47 V for 0.5 μm crack length (black curve shown in Fig. 4a). This implies that more oxygen will accumulate in the lattice of OE under higher operating voltage. The oxygen interstitial concentration decreases as the crack length increases from 0.5 to 6.5 μm, which is attributed to the combined effect of decreased partial current ratio of the DPB transport pathway and decreased overall current (see Fig. 5).

The actual oxygen vacancy concentration profile shows opposite trends compared to oxygen interstitial created by the oxygen pumping current, as plotted in Fig. 4b. Oxygen vacancy deviates the most from the equilibrium (930 mol m^{-3},[37]) for the crack length of 0.5 μm. This is because the DPB pathway contributes to a major portion of the overall current density when there is a minor crack existing at the interface. As the operating voltage increases from 1.12 to 1.47 V, the oxygen vacancy concentration decreases from 800 to 380 mol m^{-3}. Such a proportional decrease in vacancies concentration indicates high lattice oxygen non-stoichiometry in the OE under high operating voltages.

To validate the correlation between the crack length and the electrochemical performance of the cell, the current ratio (ratios of the current contribution from DPB and TPB pathways to the total current density) and the V-I curves are plotted in Fig. 5. The arrow headed lines with labels DPB and TPB indicates the variation of current ratio with increasing crack length. Figure 5a shows that for a 0.5 μm crack, the current ratio for the DPB pathway changes from 1 to 0.5 as the operating voltage increases from 1.12 to 1.47 V. Therefore, for lower operating voltages, most of the current is contributed by DPB transport pathway. As the operating voltage increases, the major contribution of current gradually transitions from the DPB to TPB pathway. As the crack length increases, the DPB current tends to decrease and approaches 0 with 6.5 μm crack length, which is consistent with the oxygen interstitial and vacancy concentration profiles shown in Fig. 4. These implies that as the crack get longer, the effective surface area between OE and EL becomes smaller that results in almost no further transfer of charged species at OE/EL interface and the oxygen stoichiometry in OE attains stable value near to equilibrium.

In Fig. 5b, the overall current density is plotted against operating voltage for different crack lengths. The overall current density at 1.47 V is reduced approximately by 76% as the crack length increases from 0.5 to 6.5 μm. Therefore, very low current generated at the DPB sites leads to smaller variation of oxygen stoichiometry from the equilibrium for longer crack length (6.5 μm) and alleviates the chemical stress failure at the interface.

J_1-integral (J m^{-2}) at the crack tip has been integrated along the contour Γ as given in Eq. 7 and plotted in Fig. 6 as a function of operating voltage under different crack lengths. With 0.5 μm crack length, the J-integral increases from 0.002 J m^{-2} to 0.018 J m^{-2} as the operating voltage increases from 1.12 to 1.47 V. Therefore, higher operating voltage leads to higher oxygen stoichiometry variation from the equilibrium, which leads to higher possibility of crack propagation. As the crack length increases, J-integral decreases nonlinearly because of the decrease in DPB current.

Table II. The physical parameters and reaction kinetics rate constants for single layer and bilayer OEs.

| Parameters	Baseline	Bilayer—10%	Bilayer—15%	Bilayer—20%	Bilayer—25%
YSZ/HE Exchange current density (ioc) [A/m^2]			2100		
GDC/LSCF Exchange current density (i$_{oa2}$) [A/m^2]	1138.44	3919.42	4002.98	4662.34	4490.69
Gas/GDC/LSCF Exchange current density (i$_{oa3}$) [A/m^2]	2801.01	5029.26	7029.53	9989.90	9489.89
Equilibrium surface oxygen coverage (θ_0)[1]			0.068		
Gas/GDC Reaction rate constant (k$_{chem}$) [mol/(m^{2}s)]			0.019		
Gas/LSCF Reaction rate constant - backward oxygen desorption (k$_{desb}$) [mol/(m^{2}s)]	0.486	0.606	0.688	0.9828	0.822
Gas/LSCF Reaction rate constant - forward oxygen desorption (k$_{desf}$) [mol/(m^{2}s)]	19.440	24.240	27.552	39.312	32.904
Gas/LSCF Reaction rate constant for oxygen evolution (k$_{evo}$) [mol/(m^{2}s)]	0.0081	0.0101	0.01148	0.01638	0.01371
Symmetry factor (β) [1]	0.491	0.662	0.407	0.444	0.515
Operating temperature (T) [K]			973.15		
Equilibrium potential (E$_{eq}$) [V]			1.05		
Chemical expansion coefficient (β^c) [m^3/mol]			1.1×10^{-6}		
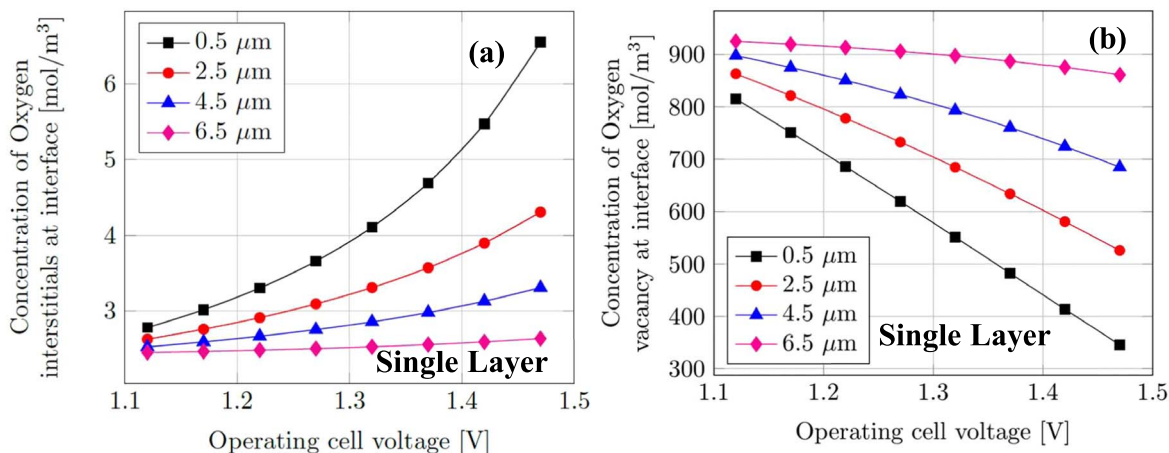
Figure 4. For the single layer design: (a) Concentration of oxygen interstitials ($c_{i,LSCF}$) at OE/EL interface, (mol/m^3); (b) Concentration of oxygen vacancies ($c_{v,LSCF}$) at OE/EL interface, (mol/m^3).
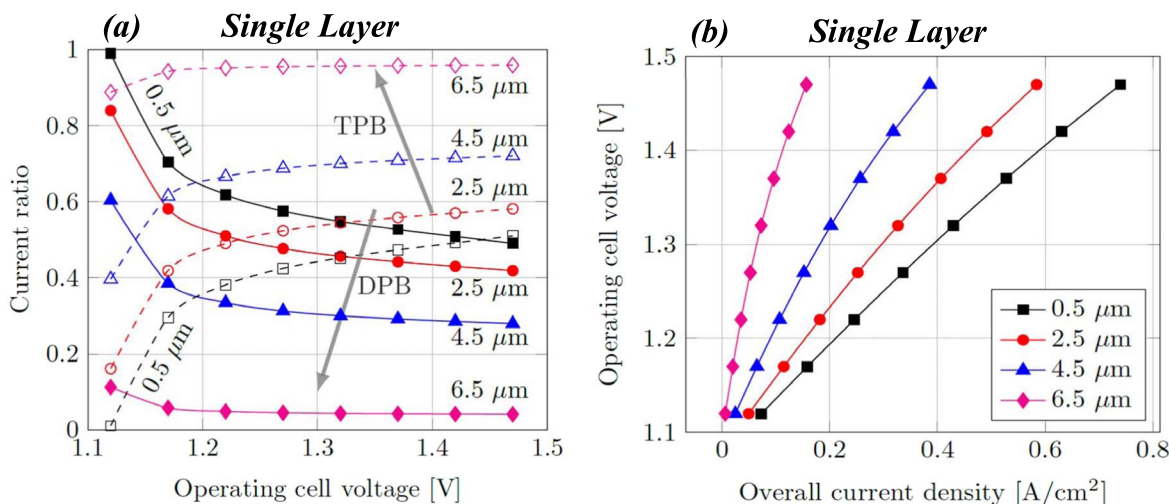

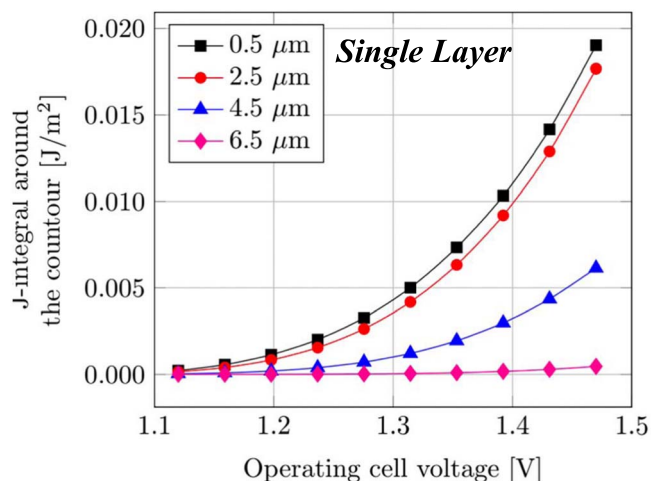**Figure 5.** For the single layer design: (a) Current Ratio; (b) Overall current density (A/m^2).

Figure 6. J-integral (J/m^2) around the crack tip for the single layer design.

Bilayer design.—In Fig. 7, the concentration of oxygen vacancy and oxygen interstitial profiles are illustrated in 2D for the bilayer design under 1.42 V and crack length of 0.5 and 6.5 μm. As shown in Figs. 7a and 7c, the concentration of oxygen vacancies becomes lowest at the OE/EL interface. When the crack grows, less current is generated by the DPB transport pathway and consequently less oxygen vacancy sites are occupied. Also, the crack disrupts the continuity along the interface, so the diffusion of oxygen vacancies is inhibited at the cracked surface. Likewise, interstitial oxygens are accumulated at the interface and their diffusion is hindered by the open crack surface, shown in Figs. 7b and 7d.

Figure 8 shows the average concentrations of oxygen interstitial and oxygen vacancies at the OE/EL interface for the bilayer design. Compared to the counterpart single layer design in Fig. 4, the following differences are noted: 1) The trends of the oxygen interstitial and oxygen vacancy profiles as a function of operating voltage are identical, but their variation range are smaller for bilayer compared to single layer. 2) With 6.5 μm crack length, both oxygen interstitial and oxygen vacancy concentration are close enough to the equilibrium value regardless of operating voltage.

Figure 9 illustrates the current ratio and overall current density for the bilayer OE design. For the bilayer design, the current ratio from the DPB pathway is seen to be enhanced under same conditions compared to the single layer design (shown in Fig. 5) due to their improved reaction kinetics. Also, the overall current density under the same operating voltage has also been enhanced approximately by 30%–50% compared against that of the single layer design. This enhancement reduces as the crack length increases.

Correspondingly, the energy release rate J$_1$-integral at the crack tip for the bilayer design in Fig. 10 is reduced by approximately
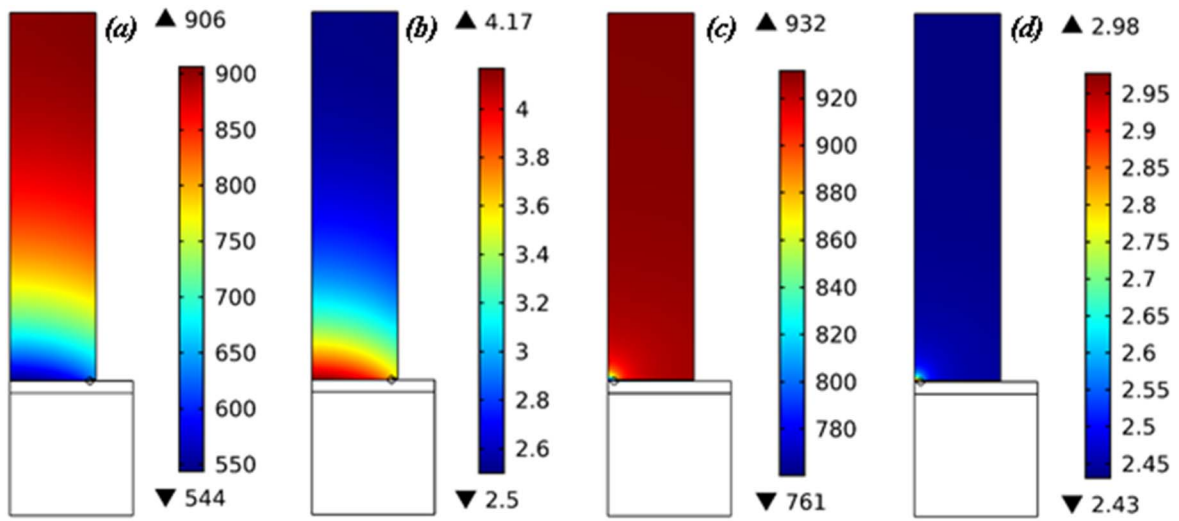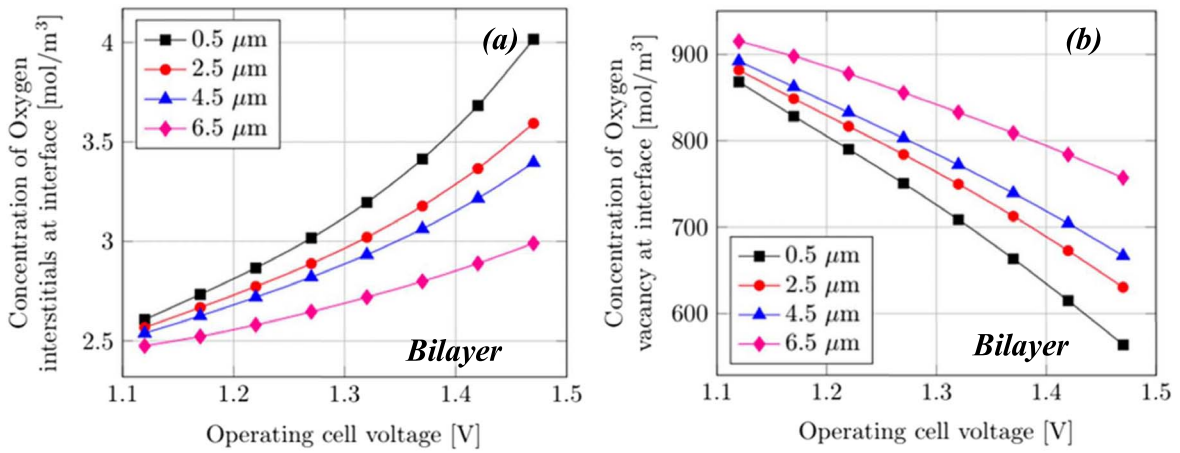
Figure 7. Concentration (mol/m^3) of Oxygen interstitials/vacancies at OE/EL interface, for the bilayer design under cell voltage of 1.42 V and crack length of 0.5μm (a) Vacancies (c$_{v,LSCF}$); (b) Interstitials (c$_{i,LSCF}$); crack length = 6.5 μm (c) Vacancies (c$_{v,LSCF}$); (d) Interstitials (c$_{i,LSCF}$).

Figure 8. For the bilayer design: (a) Concentration of oxygen interstitials (c$_{i,LSCF}$) at OE/EL interface, (mol/m^3); (b) Concentration of oxygen vacancies (c$_{v,LSCF}$) at OE/EL interface, (mol/m^3).
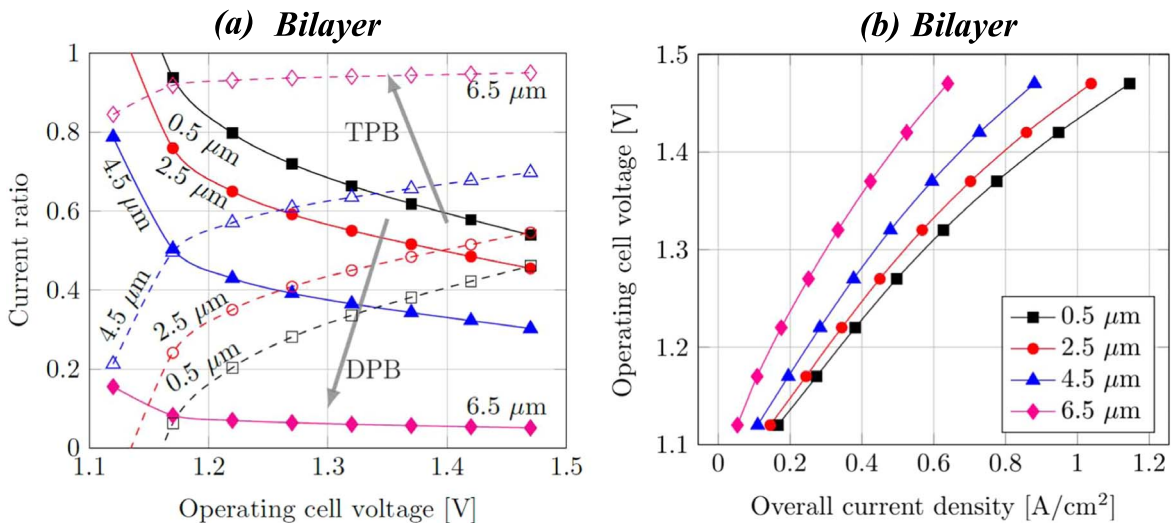

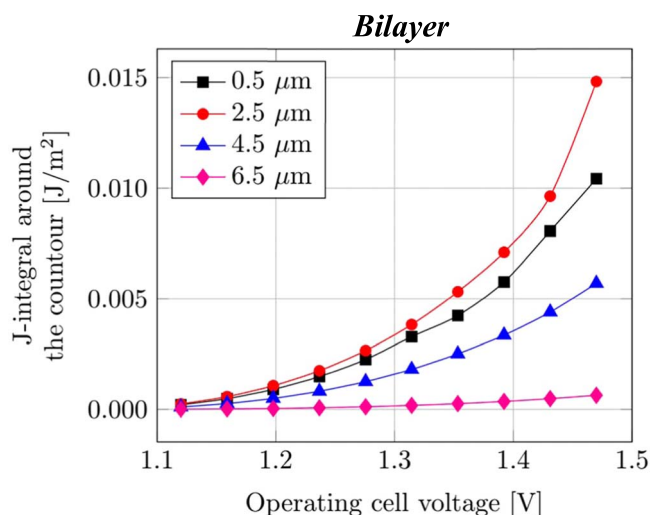**Figure 9.** For the bilayer design: (a) Current Ratio; (b) Overall current density (A/m^2).

Figure 10. J integral (J/m^2) around the crack tip for the bilayer design.

Figure 11. Experimental results of overpotential as a function of time for different OE configurations during long-term degradation tests.

25%–45% (depending upon the crack length) when compared to the single layer design in Fig. 6. The maximum J-integral value occurs at the highest operating voltage for crack lengths of 2.5 μm, which is different from that for the single layer design.

Crack growth rate.—After validating the model against the experiment data using overpotential as a function of total current density (in Experimental Validation and Model Parameters section) and studying the crack length's effect on the electrochemical performance of the cell (in Results section), experimental overpotential evolution as a function of time measured during long-term degradation tests was utilized to compute crack growth rates for different OE designs. The long-term degradation test was conducted under a fixed current density of 1 A cm^{-2}, and the experimental results are shown in Fig. 11. Researchers have associated the variation of overpotential at OE/EL interface with delamination of OE.[6] A similar approach is applied in the present scenario. The rise of overpotential with time indicates the crack propagation at OE/EL interface. The delamination process is categorized into two stages: crack initialization (where the variation of overpotential is minimal and reaches crack length of 0.05 μm by the end of this stage) and quick crack development (where the overpotential increases exponentially with time) at the interface. In the following section, we discussed how overpotential evolution with respect to time is correlated with the numerical model to obtain crack growth rates for different OE designs operated under a particular current density.

The long-term degradation test results from experiments in Fig. 11 indicate that bilayer with SCT loading 20 and 25 wt% have performed better when compared with other OE configurations. Baseline, bilayer with SCT loading of 10 wt% and 15 wt% have failed before completion of 1000 h. The only variation in these OE design configurations is SCT coating over the LSCF surface. The prior work[17] showed how SCT loading (baseline and bilayer with SCT 25 wt%) affects the lattice oxygen stoichiometry variation in the electrode. Hence, lattice oxygen stoichiometry variation especially near the electrode/electrolyte interface should be considered as one of the major contributors to degradation of electrolysis cell.

Model and experiment coupling.—Figure 12 shows step by step procedures in computing crack length and crack growth rate as functions of time by coupling numerical model and experimental data. Firstly, the numerical model validated previously is employed to predict the variation of overpotential as a function of crack length. Nonlinear variation of overpotential with crack length for different OE designs are plotted in Fig. 12a. These modeling results are used to correlate with the experimental overpotential as function of time
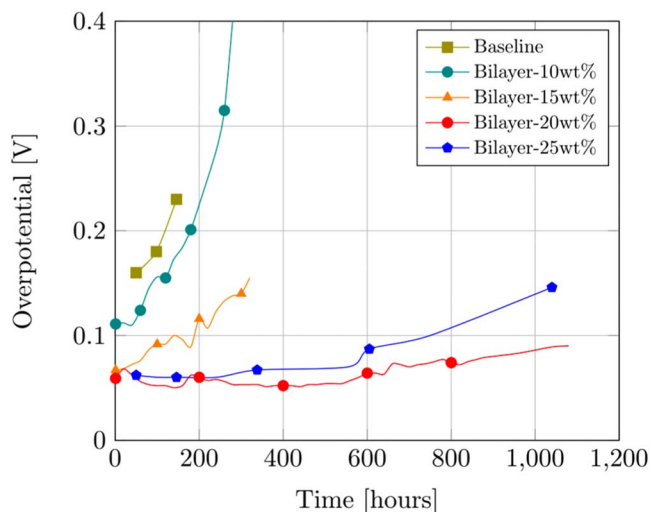
(presented in Fig. 11). For example, in the case of bilayer 20 wt% OE design, overpotential of 65 mV corresponds to crack length − 0.475 μm from the model prediction and the same overpotential was observed at 600 h during long-term test. Thus, it is hypothesized that bilayer 20 wt% SCT design will have cracked up to 0.475 μm after 600 h of operation during the fast crack development stage. Figure 12b shows graphically how the experimental measurements (symbols that plotted against right *y*-axis), and model predictions (solid line plotted against left *y*-axis) are matched up. The consolidated crack growth as a function of time for different OE designs are showcased in Fig. 12c.

Only bilayer designs with SCT loadings 20 and 25 wt% have completed the 1000 h long-term test cycle while single layer baseline design is the quickest to delaminate among all OE designs. Baseline and bilayer with SCT loadings 10 and 15 wt% have linear crack growth since the beginning, whereas bilayer 25 and 20 wt% showed no crack until 240 and 560 h respectively and this period of time is termed as crack incubation time. It is assumed that there will be no major variation in the overpotential during this period and a crack length of 0.05 μm will be initiated at OE/EL interface by the end of the incubation time. After the incubation time, crack grows linearly like other OE designs, and it is categorized as quick crack development period.

Figure 12d presents crack growth rate derived from the simulation results for bilayer OE configurations. SCT—10 wt% bilayer has the faster crack growth rate of 0.032 μm/hr at the beginning and gradually reduces as it reaches complete delamination of OE/EL interface. The lowest crack growth rate was experienced by SCT—20 wt% bilayer, which is about 0.005 μm/hr and the rate is negligible in the first 560 h during the crack incubation time. This confirms that this bilayer configuration has a longer lifetime to operate before complete delamination. Thus, SCT coating on LSCF improves the electrochemical performance and mechanical stability of the cell.

Failure criteria-stress intensity factor.—In this study, J-integral is used to compute the fracture criteria for OE/EL interface, as defined in J integral section. The stress intensity factor (SIF) K_I is calculated by Eqs. 7–10. The stress intensity factor due to chemical induced stress at OE/EL interface as a function of crack length is shown in Fig. 13 for different OE configurations under 1 A cm^{-2}. Baseline LSCF single layer design shows the highest SIF under various crack lengths, whereas SCT 20 wt% - LSCF bilayer design shows the lowest SIF across all crack length. The SIF increases tremendously and attains a peak value when crack length is near 3
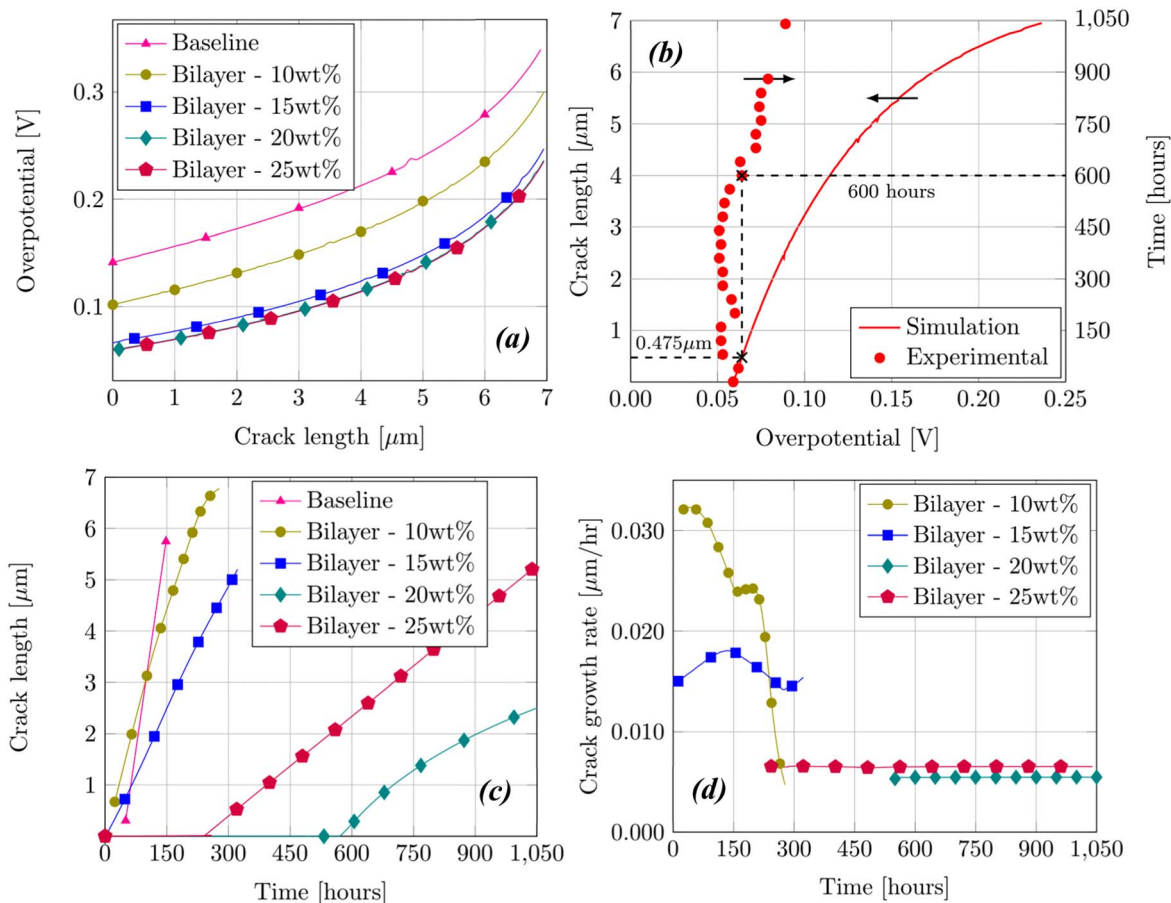
Figure 12. (a) Simulated overpotential as a function of crack length, (b) correlation of crack length vs time for 20%SCT/LSCF bilayer design, (c) crack length evolution as a function of time for different OE configurations, and (d) crack growth rate for bilayer OE configurations.
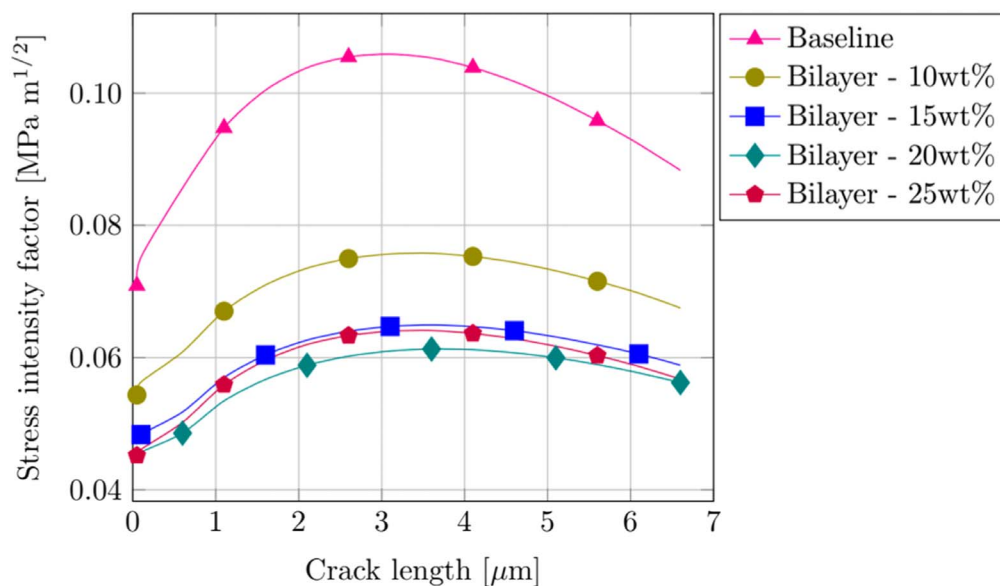

Figure 13. Stress intensity factor due to chemical stress as a function of crack length for different OE configurations.

μm, and then drops slightly until the crack length reaches the maximum limit. As crack length increases, current contribution from TPB becomes dominant, and this reduces the migration of oxygen ions through OE/EL interface. This explains the decreasing trend of SIF as crack length increases after the peak value. OE configurations with lower stress intensity factor will have slower crack growth rate.

Model predictions.—The SCT 20wt%-LSCF bilayer design is selected as the optimal OE for further investigation of cell performance at other current densities. Paris law defines the relation between SIF and crack growth per cycle for cyclic fatigue loads.[30,38] Similarly, creep crack growth rate relationship with time can be stated analogous to Paris law[39,40] as
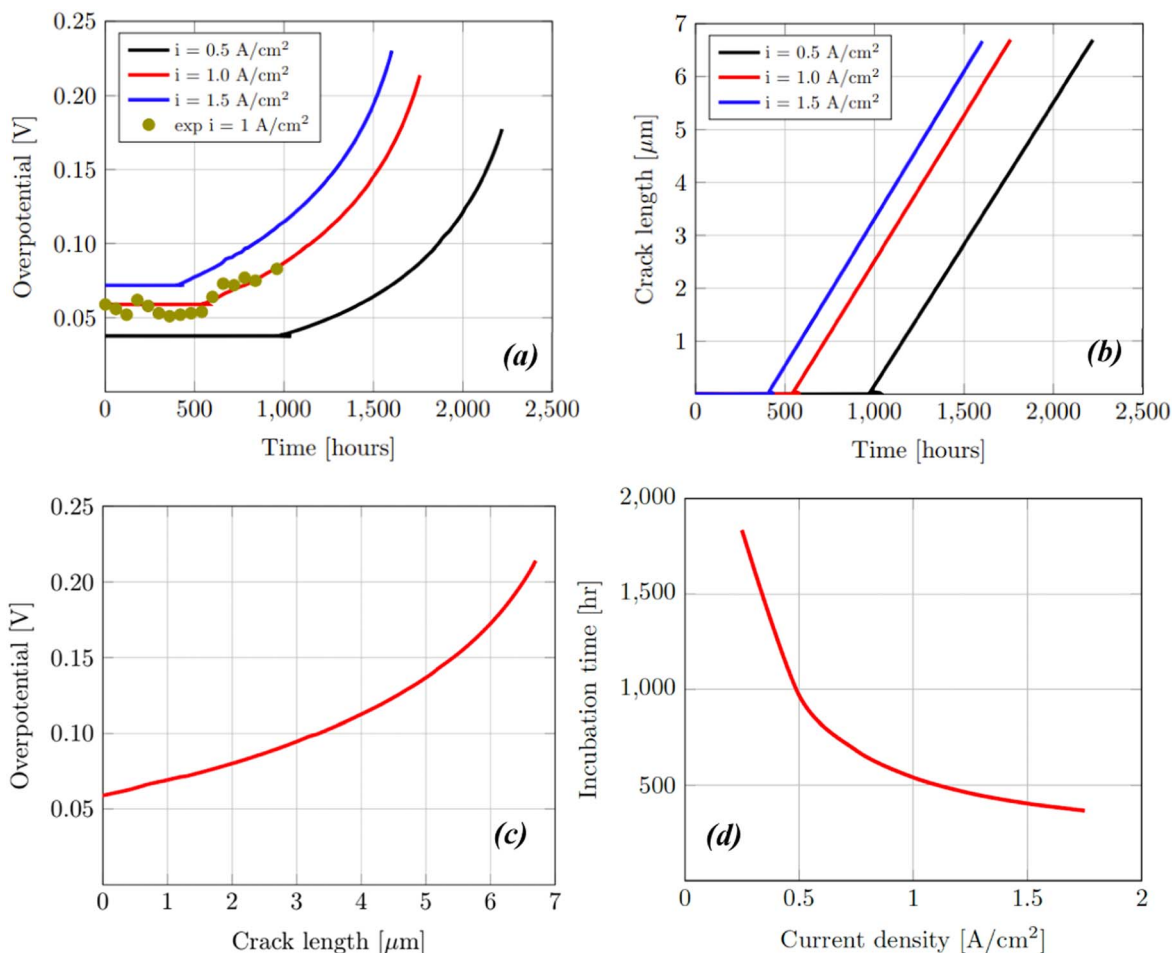
Figure 14. Overpotential (a) and crack length (b) as a function of time for different current densities, overpotential as function of crack length (c) and incubation time under different current densities (d) for SCT20%-LSCF bilayer design using model prediction.

$$\frac{da}{dt} = C(K_I)^m \qquad [12]$$

where C and m are unknown coefficient which are to be derived, K_I is stress intensity factor and a is crack length at time t. Since the crack length as a function of time for a particular current density is already established in previous section, coefficients C and m are obtained. As discussed earlier, there are two crack growth periods: 1) incubation period and 2) quick crack development period. Therefore, Eq. 12 is applied separately for each period, i.e., there are totally four coefficients: C1 and m1 for the incubation period, and C2 and m2 for the quick crack development period. When all four coefficients are available, it is feasible to estimate crack growth as a function of time for other current densities since these estimated coefficients are material properties and independent of operating conditions.

Figure 14a presents overpotential predicted for SCT-20wt% bilayer OE design beyond the experimental time until delamination of OE/EL takes place for current densities 0.5, 1.0 and 1.5 A cm^{-2}. The crack length growth as a function of time for the bilayer design operated under different current densities are shown in Fig. 14b. Cells operated at lower current densities takes longer time to reach full delamination. Under 1 A cm^{-2}, the cell could operate for up to 1750 h before complete delamination. Overpotentials before delamination are different under different current densities. Therefore, the overpotential is not necessarily a good indicator that comprehensively specifies the failure of the cell irrespective of configurations. The crack growth varies linearly with time after incubation time.

This is because the overpotential has exponential variation with crack length from the model as presented in Fig. 14c and concurrently, overpotential increase exponentially in time during long-term test after crack initiated (as seen in Fig. 11) which makes linear variation of crack with respect to time. Figure 14d gives the relationship between incubation time and current density, where the incubation time is shown to decrease exponentially as current density increases.

Discussions.—According to open literature, critical SIF (also called fracture toughness of the material) has been reported to vary in range of 0.54 and 3 MPa·m$^{1/2}$,[6,13,16,41] for dense OE materials. It was also stated in literature that LSCF material in microscale has apparently lower SIF value of 0.17 MPa· m$^{1/2}$ while compared to the bulk material of similar porosity.[41] In the current model, the maximum SIF is predicated close to 0.10 MPa·m$^{0.5}$ for baseline OE design, which is primarily based on the lattice stoichiometry variation caused compression in LSCF. Under high temperature electrolysis mode, the OE could also experience stresses caused by other factors, such as thermal residual stress and oxygen partial pressure build-up.

If the thermal residual stress was considered, thermal stresses generated from a temperature difference between the sintering temperature and operating temperature should be added in the Solid Mechanics model of the multilayer structure.[28,42] The residual thermal stress becomes superimposed with chemical-induced stress, as both stresses are compressive in nature and increases the

possibility of failure. The point has been further elaborated in Appendix B.

For sake of argument if oxygen pressure built-up in the enclosed pores at the interface should be considered to analyze the delamination, then it could not explain how quickly the crack will grow with different OE configurations. With the same LSCF backbone but different SCT loadings, the baseline cell has failed near 150 h, bilayer with SCT 10 wt% near 260 h and SCT 15 wt% near 320 h. In the experimental data shown in Fig. 11, degradation occurs much earlier than the critical overpotential of 200 mV, which is the threshold overpotential value for stable operation of electrolyzer cell computed based on pressure and corresponding stress intensity factor from the literature.[6,8,13]

The above statement validates our motivation to focus on the chemical-induced stress as the primary driving force for failure of the OE design configurations. And SCT layer mitigates the lattice oxygen variation by enhancing the oxygen evolution reaction kinetic rate at the electrode surface. Hence, increasing the SCT loading has enhanced the performance and lifetime of the cell. However, based on the low SIF obtained in the research, we think that 1) the lattice of OE must be affected by its operating condition and surface reaction kinetics, so we could improve the mechanical integrity of the cell by improving the electrokinetics of the OE surface; 2) the interface delamination must be caused by a combined effect from chemical compression in the lattice, thermal residual stress from temperature differences and oxygen partial pressure buildup in the enclosed pores; 3) Failure criteria based on critical overpotential from the literature, due to oxygen partial pressure built up in the enclosed pore, contradicts with the experimental observations in this research. Therefore, a better indicator considering changes in both the pores and in the lattice under high polarization is needed, which will be our future research.

Summary

To summarize, this work presents an electro-chemical-mechanical coupled model that computationally connects cell performance with delamination of different OEs under various current densities. From the initial analysis, it is found that SCT coating on LSCF improves the overall cell performance when compared to baseline single layer design, as this OER-active coating layer improves the reaction kinetics at DPB transport pathway.

The model's predictions and experimental data have been successfully coupled to correlate and predict crack length and its growth rate as a function of time. It is shown that the SCT 20wt %-LSCF bilayer design is the optimal configuration with the slowest crack growth rate and best cell performance under various conditions. Furthermore, model prediction of crack growth and overpotential for different current densities is computed for the optimal SCT-20wt% bilayer design. The analysis shows that cells operated at lower current density will have longer incubation time and slower crack growth. Under 1 A cm^{-2}, the cell could operate for up to 1750 h before full delamination. Finally, the thermal residual stress is additive with the chemical induced stress, as both the stresses are compressive in nature. Overpotentials before fatal failure of the cell are different under different current densities, therefore, it is not a good indicator to comprehensively specify the failure of the cell irrespective of configurations. We will search for a better failure indicator in our future research.

Acknowledgments

Appendix A. Optimization of Unknown Parameters with Synthetic and Experimental Data

Figure A·1 gives the scaled sensitivity of the parameters individually for both intact and cracked cell as function of current density. Irrespective of their magnitudes, the parameters show variation in their sensitivity trends as the crack propagates at the electrode interface, implying that these parameters are influenced by
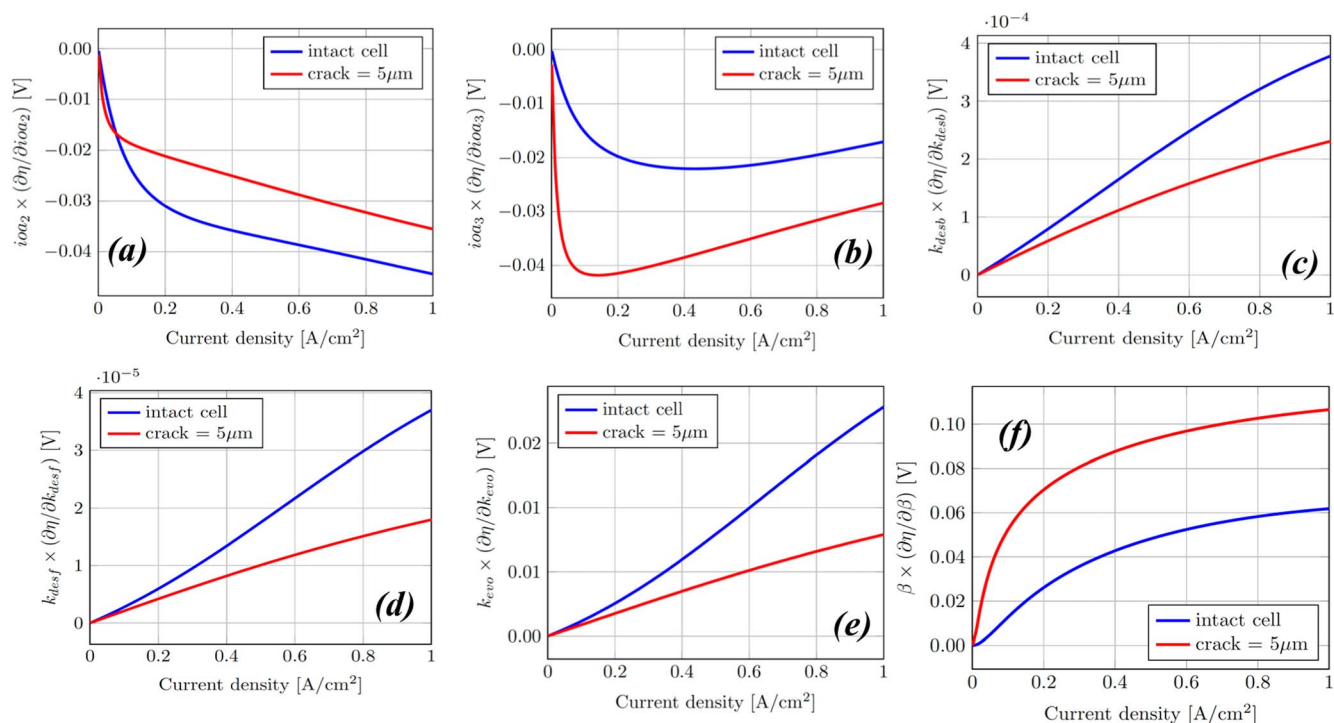

Figure A·1. Normalized sensitivity profiles for fresh cell and degraded cell with 5 μm crack with respect to DPB exchange current density (a), TPB exchange current density (b), oxygen desorption rate forward (c) and backward (d), oxygen evolution rate (e) and symmetry factor (f).
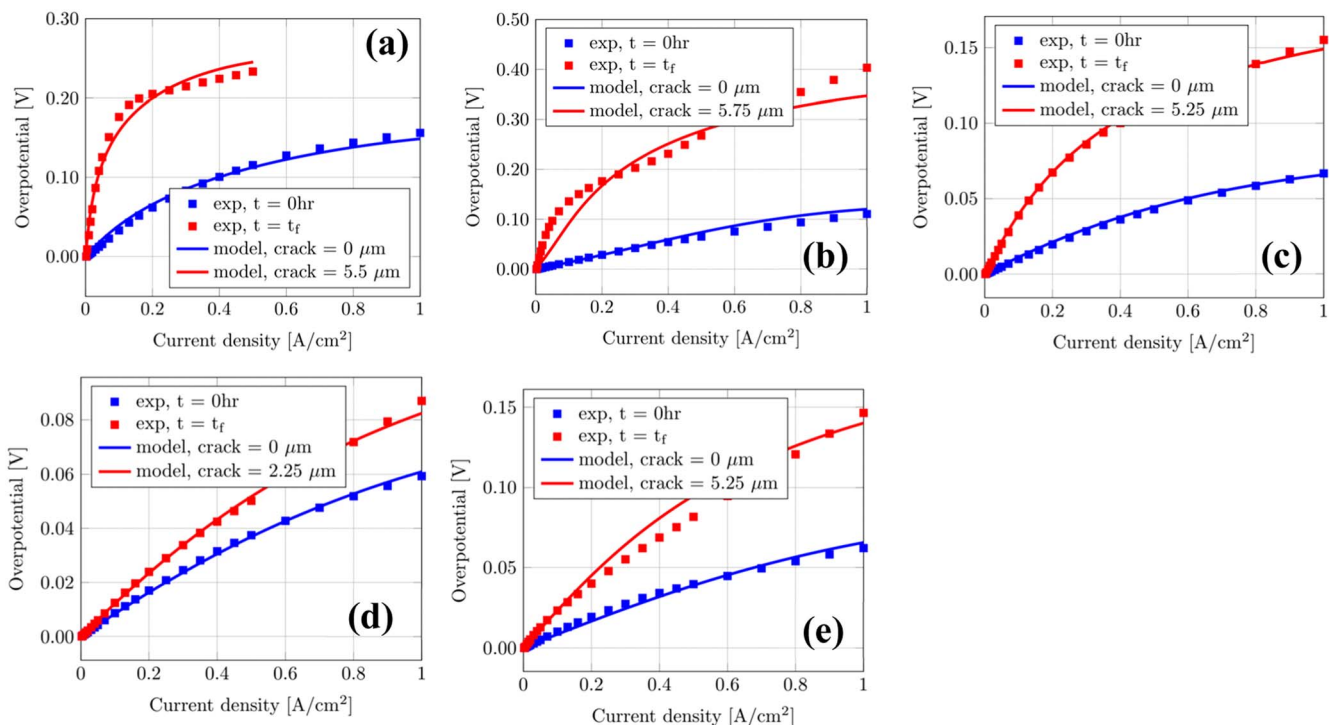
Figure A·2. Comparison of VI curves of experiment and model simulation from inverse solution for different OEs– baseline (a), bilayer 10wt% (b), bilayer 15wt% (c), bilayer 20wt% (d) and bilayer 25wt% (e).
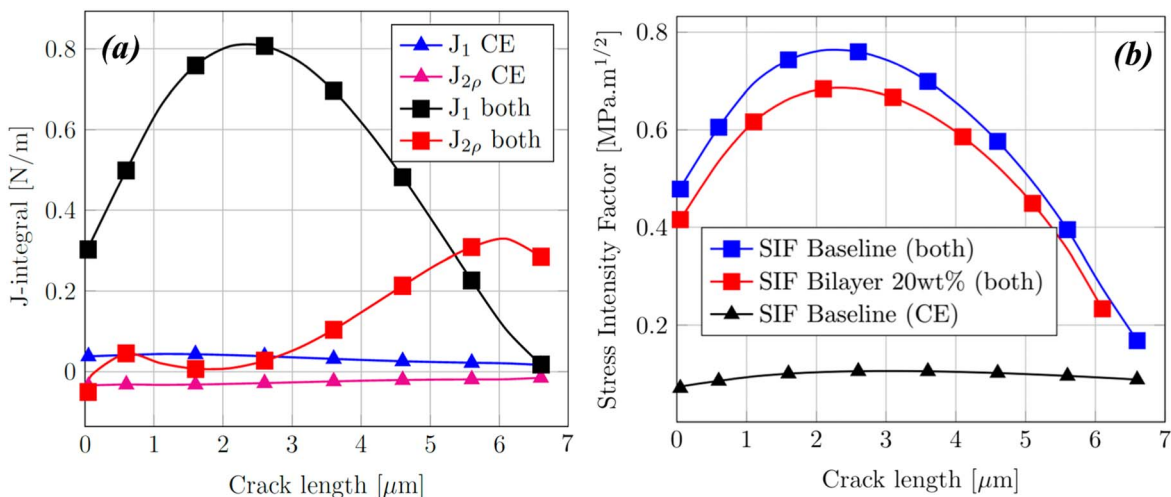

Figure A·3. J-integral (a) and stress intensity factor (b) comparison for model under chemical-induced stress with and without thermal residual stress.

Table A·1. Correlation matrix.

Parameter	i_{oa2}	i_{oa3}	k_{desb}	k_{desf}	k_{evo}	β
i_{oa2}	1.0000	−0.5099	−0.9805	−0.9601	−0.9477	0.0428
i_{oa3}	—	1.0000	0.4847	0.5157	0.5262	−0.7269
k_{desb}	—	—	1.0000	0.9910	0.9826	0.0148
k_{desf}	—	—	—	1.0000	0.9986	−0.0477
k_{evo}	—	—	—	—	1.0000	−0.0733
β	—	—	—	—	—	1.0000

the crack growth. The inference made from Fig. A·1 is the parameters like exchange current density at DPB and TPB, oxygen evolution reaction rate constant and symmetry factor are feasible to estimate simultaneously.

Correlation analysis is performed to investigate if any correlation between the sensitive parameters exists. If the parameters are highly correlated, then it becomes a tedious task to obtain a unique set of parameters through optimization. The correlation matrix shown in

Table A·2. Optimization results for Inverse problem performed with synthetic data.

Parameter	Initial guess	Exact value	Noiseless		With Noise	
			Estimated	error %	Estimated	error %
i_{oa2}	80.00	800.00	799.834	0.021	730.991 ± 59.97	8.62
i_{oa3}	160.00	1600.00	1600.16	0.010	1408.71 ± 84.87	11.95
k_{evo}	0.0012	0.01206	0.01205	0.096	0.01362 ± 0.0025	12.98
β	0.028	0.28	0.28001	0.002	0.271 ± 0.0071	2.91

Table A·1, is calculated using following relation,[43]

$$r(\alpha_i, \alpha_j) = \frac{cov(\alpha_i, \alpha_j)}{\sqrt{var(\alpha_i)var(\alpha_j)}} \qquad [A·1]$$

Here $cov(\alpha_i, \alpha_j)$ represents covariance function between parameter α_i and α_j and $var(\alpha_i)$ denotes variance function for the parameter α_i. The table shows that DPB exchange current density is highly correlated with reaction kinetics of oxygen desorption and evolution rates (since their absolute magnitude is more than 0.9). To separate the influence of reaction rates over exchange current density, two VI curves are used; one measured from the fresh cell and the other one from the degraded cell measured before complete failure during the long-term test. This approach increases the accuracy of the optimized parameters.

Before proceeding with the optimization using the experimental measurements, synthetic data is used for understanding the mathematical model. The case study is performed only for baseline OE configuration with VI profiles obtained for fresh and degraded cell (of presumed crack length = 5 μm). Table A·2 shows the results of inverse problems using synthetic data. Without noise, it was possible to get back almost the exact parameters with error less than 0.1%. For synthetic run with 5% noise level, it was feasible to retrieve the parameters with maximum error of 13% for each parameter. This case study provides confidence on the optimization techniques that will be used to solve the inverse problem using the experimental data. From sensitivity and correlation analysis backed with synthetic data case study, we concluded that it is feasible to approximate the sensitive parameters like exchange current densities at DPB (i_{oa2}) and TPB (i_{oa3}), oxygen evolution reaction kinetics (k_{evo}), symmetry factor (β), from VI curves for fresh and degraded cell. Figure A·2 shows the agreement of the inverse solution with the experimental measurement for different OE configurations. Only VI curve for cracked bilayer 10 wt% cell has some discrepancies between model and measurements while other configurations show good agreements.

Appendix B. Influence of Thermal residual Stress on J-integral and Stress Intensity Factor

Residual stress in an electrode material is induced attributed to high temperature fabricating process.[28,42] The magnitude of the residual stress becomes significant if the electrode is operated at a lower temperature than the sintering temperature.[42] Moreover, the residual stress affects the crack initiation/propagation and eventually stress intensity factor (SIF).[28] The chemical-induced stress due to concentration gradient in the electrode, presented in this study earlier, is superimposed with the pre-existing thermal residual stress and both are compressive in nature. In the model here, we assumed that the sintering temperature is 1000 °C and the operating temperature is 700 °C.

Figure A·3 presents the updated J-integral around the crack tip and SIF as functions of crack length for baseline OE configuration operated under current density 1 A cm^{-2}, including J_1 and J_2 computed using Eqs. 7 and 8, respectively. Figure A·3a illustrates that the baseline electrode under chemical stress (CE) exhibits lower J-integral values near crack tip when compared to electrode under both chemical and thermal residual stress. J_2 comprises of energy releases rate near crack tip and energy jump at the interface and crack. The signs of J_2 for both cases are changed due to the mismatch in thermal expansion coefficients for the materials LSCF and GDC. Figure A·3b also shows that SIF for the baseline electrode with both stresses is almost 6 times more than the electrode with only chemical stress. SIF for the electrode with both stresses has exceeded the fracture toughness of LSCF.

In the present study, it was assumed that crack initiates and propagates at the LSCF/GDC interface. Since the baseline materials for the electrode (LSCF) and buffer layer (GDC) are common for all the configurations studied in this work, the thermal residual stress must be the same irrespective of OE designs. In Fig. A·3b, SIF for bilayer 20 wt% at any crack length is approximately 10% lower than baseline OE owing to their lower chemical-induced compressive stress, which resulted in a much lower crack growth rate.

ORCID

Puvikkarasan Jayapragasam https://orcid.org/0000-0003-2377-5557
Jacob A. Wrubel https://orcid.org/0000-0002-3347-0768
Kevin Huang https://orcid.org/0000-0002-1232-4593
Xinfang Jin https://orcid.org/0000-0002-3148-4904

References

1. A. Nechache and S. Hody, "Alternative and innovative solid oxide electrolysis cell materials: a short review." *Renew. Sustain. Energy Rev.*, **149**, 111322 (2021).
2. M. Reisert, A. Aphale, and P. Singh, "Solid oxide electrochemical systems: material degradation processes and novel mitigation approaches." *Materials*, **11**, 2169 (2018).
3. F. Monaco, D. Ferreira-Sanchez, M. Hubert, B. Morel, D. Montinaro, D. Grolimund, and J. Laurencin, "Oxygen electrode degradation in solid oxide cells operating in electrolysis and fuel cell modes: LSCF destabilization and interdiffusion at the electrode/electrolyte interface." *Int. J. Hydrogen Energy*, **46**, 31533 (2021).
4. Kevin Huang and B. John, *Goodenough., Solid oxide fuel cell technology. Principle, perfromance and operations* (Boca Raton, FL, CRC Press) (2009).
5. Y. Matsuzaki and I. Yasuda, "Dependence of SOFC cathode degradation by chromium-containing alloy on compositions of electrodes and electrolytes." *J. Electrochem. Soc.*, **148**, A126 (2001).
6. B. K. Park, Q. Zhang, P. W. Voorhees, and S. A. Barnett, "Conditions for stable operation of solid oxide electrolysis cells: oxygen electrode effects." *Energy Environ. Sci.*, **12**, 3053 (2019).
7. L. Zhang, L. Zhu, and A. V. Virkar, "Modeling of oxygen chemical potential distribution in solid oxide electrolyzer cells." *J. Electrochem. Soc.*, **166**, F1275 (2019).
8. A. V. Virkar, "Mechanism of oxygen electrode delamination in solid oxide electrolyzer cells." *Int. J. Hydrogen Energy*, **35**, 9527 (2010).
9. Office, 'D.H.a.F.C.T. 3rd Annual HydroGEN Advanced Water Splitting Technology Pathways Benchmarking and Protocols Workshop (2021).
10. K. Chen and S. P. Jiang, "Failure mechanism of (La,Sr)MnO3 oxygen electrodes of solid oxide electrolysis cells." *Int. J. Hydrogen Energy*, **36**, 10541 (2011).
11. S. N. Rashkeev and M. V. Glazoff, "Atomic-scale mechanisms of oxygen electrode delamination in solid oxide electrolyzer cells." *Int. J. Hydrogen Energy*, **37**, 1280 (2012).
12. P. Moçoteguy and A. Brisse, "A review and comprehensive analysis of degradation mechanisms of solid oxide electrolysis cells." *Int. J. Hydrogen Energy*, **38**, 15887 (2013).
13. A. V. Virkar, "Failure of Ion-conducting materials by internal precipitation under electrolutic conditions." *Engineered Ceramics: Current Status and Future Prospects* (The American Ceramic Society and Wiley) 59 (2016).
14. B. N. Nguyen, B. J. Koeppel, S. Ahzi, M. A. Khaleel, and P. Singh, "Crack growth in solid oxide fuel cell materials: from discrete to continuum damage modeling." *J. Am. Ceram. Soc.*, **89**, 1358 (2006).

15. R. Knibbe, M. L. Traulsen, A. Hauch, S. D. Ebbesen, and M. Mogensen, "Solid oxide electrolysis cells: degradation at high current densities." *J. Electrochem. Soc.*, **157**, B1209 (2010).

16. J. G. Railsback, H. Wang, M. Y. Lu, and S. A. Barnett, "Degradation of La0.6Sr0.4Fe0.8Co0.2O3-δoxygen electrodes on Ce0.9Gd0.1O2-Δelectrolytes during reversing current operation." *J. Electrochem. Soc.*, **164**, F3083 (2017).

17. K. Cook, J. Wrubel, Z. Ma, K. Huang, and X. Jin, "Modeling electrokinetics of oxygen electrodes in solid oxide electrolyzer cells." *J. Electrochem. Soc.*, **168**, 114510 (2021).

18. F. Tietz, D. Sebold, A. Brisse, and J. Schefold, "Degradation phenomena in a solid oxide electrolysis cell after 9000 h of operation." *J. Power Sources*, **223**, 129 (2013).

19. G. Schiller, A. Ansar, M. Lang, and O. Patz, "High temperature water electrolysis using metal supported solid oxide electrolyser cells (SOEC)." *J. Appl. Electrochem.*, **39**, 293 (2009).

20. Y. Lu, C. Kreller, and S. B. Adler, "Measurement and modeling of the impedance characteristic of porous La$_{1-x}$ Sr$_x$ CoO$_{3-\delta}$ electrodes." *J. Electrochem. Soc.*, **156**, B513 (2009).

21. S. J. Kim and G. M. Choi, "Stability of LSCF electrode with GDC interlayer in YSZ-based solid oxide electrolysis cell." *Solid State Ionics*, **262**, 303 (2014).

22. N. Minh, J. Mizusaki, and S. C. Singhal, "Advances in solid oxide fuel cells: review of progress through three decades of the international symposia on solid oxide fuel cells." *ECS Trans.*, **78**, 63 (2017).

23. P. S. Jørgensen, K. Y.- Kremski, J. Wilson, J. R. Bowen, and S. Barnett, "On the accuracy of triple phase boundary lengths calculated from tomographic image data." *J. Power Sources*, **261**, 198 (2014).

24. A. Hammou and S. Georges, *Solid-State Electrochemistry: Essential Course Notes and Solved Exercises* (Switzerland AG, Springer Nature) (2020).

25. X. Jin, "Modeling of chemical-mechanical couplings in solid oxide cells." *PhD Thesis*, University of South Carolina (2014).

26. N. Swaminathan and J. Qu, "Interactions between non-stoichiometric stresses and Defect Transport in a Tubular Electrolyte." *Fuel Cells*, **7**, 453 (2007).

27. S. Timoshenko and J. N. Goodier, *Theory of Elasticity* (McGraw-Hill, New York) (1970).

28. H. E. Coules, G. C. M. Horne, K. Abburi Venkata, and T. Pirling, "The effects of residual stress on elastic-plastic fracture propagation and stability." *Mater. Des.*, **143**, 131 (2018).

29. F. G. Gaudette, A. Giannakopoulos, and S. Suresh, "Interface cracks in layered materials subjected to a uniform temperature change." *Int. J. Fract.*, **110**, 325 (2001).

30. A.-R. Ragab and S. E. Bayoumi, *Engineering Solid Mechanics: Fundamentals and Applications* (Boca Raton, FL, CRC Press).

31. Z. Suo and J. W. Hutchinson, "Interface crack between two elastic layers." *Int. J. Fract.*, **43**, 1 (1990).

32. R. E. Smelser and M. E. Gurtin, "On the J-integral for Bi-material bodies." *Journal of Fracture*, **13**, 382 (1977).

33. R. Khandelwal and J. M. C. Kishen, "Complex variable method of computing Jk for bi-material interface cracks." *Eng. Fract. Mech.*, **73**, 1568 (2006).

34. J. Scheel and A. Ricoeur, "A comprehensive interpretation of the J-integral for cohesive interface cracks and interactions with matrix cracks." *Theor. Appl. Fract. Mech.*, **100**, 281 (2019).

35. K. C. Nehar, B. E. K. Hachi, F. Cazes, and M. Haboussi, "Evaluation of stress intensity factors for bi-material interface cracks using displacement jump methods." *Acta Mechanica Sinica/Lixue Xuebao*, **33**, 1051 (2017).

36. P. Jayapragasam, P. L. Bideau, and T. Loulou, "Computing sensitivity coefficients by using complex differentiation: Application to heat conduction problem." *Numerical Heat Transfer, Part B: Fundamentals*, **74**, 729 (2018).

37. S. S. Hashimoto, Y. Fukuda, M. Kuhn, K. Sato, K. Yashiro, and J. Mizusaki, "Oxygen nonstoichiometry and thermo-chemical stability of La0.6Sr0.4Co1-yFeyO3-δ (y = 0.2, 0.4, 0.6, 0.8)." *Solid State Ion*, **181**, 1713 (2010).

38. N. M. Pugno, M. Ciavarella, P. Cornetti, and A. Carpinteri, "A generalized paris' law for fatigue crack growth." *J. Mech. Phys. Solids*, **54**, 1333 (2006).

39. F. W. Brust, G. M. Wilkowski, P. Krishnaswamy, and K. Wichman, "Creep and creep-fatigue crack growth at structural discontinuities and welds." *ASME Standards Technology*, DOE/ID14712-8 (2010), New York.

40. W. P. Foo and R. Castillo, "Fracture mechanics approach to creep crack growth in welded in738lc gas turbine blades." *J. Eng. Gas Turbines Power*, **114**, 275 (1992).

41. Z. Chen, X. Wang, F. Giuliani, and A. Atkinson, "Fracture toughness of porous material of lscf in bulk and film forms." *J. Am. Ceram. Soc.*, **98**, 2183 (2015).

42. K. Huang and D. H. Harter, "Temperature-dependent residual stresses in plasma sprayed electrolyte thin film on the cathode substrate of a solid oxide fuel cell." *Solid State Ionics*, **181**, 943 (2010).

43. A. Adili, N. Hasni, C. Kerkeni, and S. B. Nasrallah, "An inverse problem based on genetic algorithm to estimate thermophysical properties of fouling." *Int. J. Therm. Sci.*, **49**, 889 (2010).